Materials International
Open Access Journal (ISSN: 2668-5728)

Article
Volume 7, Issue 1, 2021, 5
https://doi.org/10.33263/Materials71.005

Modulation of the Normalized Intersubband Transition Energy of *GaAs* Quantum Dot under the Influence of Noise and Anharmonicity

Bhaskar Bhakti [1], Manas Ghosh [1,*]

[1] Department of Chemistry, Physical Chemistry Section, Visva-Bharati University, Santiniketan, Birbhum-731235, West Bengal, India; bhaskarbhakti2016@gmail.com;
* Correspondence: manasghosh.chem@visva-bharati.ac.in/ pcmg77@gmail.com;

Scopus Author ID 8258661600
Received: 19.09.2024; Accepted: 2.01.2025; Published: 13.02.2025

Abstract: The present inquiry minutely inspects the intersubband transition energy (ISTE) and the normalized intersubband transition energy (NISTE) of GaAs quantum dot (QD) under the direct influence of Gaussian white noise present in the dot confinement potential. The various features of the ISTE and NISTE plots against the variations of different physical parameters depend on the presence/absence of noise and the mode of entrance (additive and multiplicative) of noise. These features comprise steady growth, steady fall, maximization, minimization, and change in the relative magnitudes of ISTE and NISTE. Moreover, when the presence of *anharmonicity* in the QD confinement is considered, it comes out that the symmetry (odd/even) and the strength of the anharmonic potential also modulate the ISTE and the NISTE profiles. Throughout the entire study, the NISTE plots unveil their greater efficacy over the ISTE plots in realizing the effects of various physical quantities. The study's findings may shed light on the optical properties of low-dimensional nanostructures under the influence of noise and in the presence of anharmonicity.

Keywords: quantum dot; anharmonicity; Gaussian white noise; intersubband transition energy; normalized intersubband transition energy.

1. Introduction

Progresses in semiconductor nanotechnology in the last three decades have become able to produce low-dimensional nanostructures such as quantum wells (QWLs), quantum wires (QWRs), quantum well wires (QWWs), and quantum dots (QDs). These low-dimensional nanostructures are highly acclaimed thanks to their role in realizing basic physics and profound usage in various microelectronic, optoelectronic, and photonic devices.

External perturbations such as applied electric field, magnetic field, temperature, pressure, etc., noticeably influence the electronic and optical properties of low-dimensional nanostructures. As a result, the properties of these systems can be regulated. This has serious implications in terms of manufacturing new devices and improving the output of existing ones [1–22]. Added to this, the doping of impurities also tremendously affects the electronic and optical properties of low-dimensional nanostructures [2,3,5–8,23–41].

Exploration of transition energies merits importance owing to its immense significance in elucidating the optical properties of the system. During the intersubband transition, the electron gets stimulated by external radiation and is promoted from one energy level to another

within the conduction band or the valence band. The consequent optical absorption and the oscillator strength bear considerable significance in condensed matter physics. The operating wavelength of the intersubband devices possesses ample scope for wavelength regulation by proper design. Remarkable efforts have been made to accomplish the operating wavelength relevant to the telecommunication spectral ranges residing within 1.3 μm and 1.55 μm. Thus, the intersubband technology undergoes rigorous applications in the near-infrared regime and bears the possibility of further expansion to the mid-infrared terahertz range, giving rise to the fabrication of infrared detectors [42,43]. Consequently, the last few decades have witnessed sufficient research related to the intersubband transitions in low-dimensional nanostructures [1,4,6,23–26,42–54].

The current study strives to make a comprehensive inspection of the intersubband transition energy (ISTE) [47,48,54] and normalized intersubband transition energy (NISTE) [47,54] of GaAs QD under the influence of Gaussian white noise. NISTE appears more advantageous than ISTE since the former can illuminate some feeble features that may not be observed in the ISTE profiles [47,54]. The QD confinement comprises lateral parabolic potential, which restricts the electronic motion to the x – y surface in space, a perpendicular magnetic field, an applied static electric field in x and y directions, and noise. The noise contribution comes out to be different depending on its mode of ingression (additive/multiplicative). As a special case of substantial importance, at the end of the discussion, we have also envisioned the presence of anharmonicity (of odd and even parities) in the QD confinement potential. The study scrutinizes the ISTE and the NISTE profiles, pursuing the change of several physical parameters over a range, considering and ignoring noise. The characteristics of the ISTE and the NISTE profiles manifest the viability of harnessing the optical transitions of GaAs QD in a targeted manner by proper control over various physical quantities, parity, and strength of anharmonicity, as well as noise.

2. Materials and Methods

Under the effective mass approximation, the QD Hamiltonian, including the lateral parabolic confinement, lateral electric field, vertical magnetic field, and noise, becomes

$$H_0 = H_0' + V_{imp} + |e|F(x+y) + \xi(x,y) \qquad (1)$$

H_0' contains the basic parabolic confinement $\frac{1}{2}m^*\omega_0^2(x^2+y^2)$ and the magnetic field contributes and reads

$$H_0' = \frac{1}{2m^*}\left[-i\hbar\nabla + \frac{e}{c}\boldsymbol{A}\right]^2 + \frac{1}{2}m^*\omega_0^2(x^2+y^2) \qquad (2)$$

with ω_0, m and $\boldsymbol{A}$ represent the confinement frequency, the electronic effective mass, and the vector potential [given by A = (By,0,0) in Landau gauge where B is the magnetic field strength]. H_0' then turns out to be

$$H_0' = -\frac{\hbar^2}{2m^*}\left(\frac{\partial^2}{\partial x^2} + \frac{\partial^2}{\partial y^2}\right) + \frac{1}{2}m^*\omega_0^2x^2 + \frac{1}{2}m^*\Omega^2y^2 - i\hbar\omega_c y\frac{\partial}{\partial x} \qquad (3)$$

ω_c and $\Omega\left(=\sqrt{\omega_0^2+\omega_c^2}\right)$ are the cyclotron frequency and the gross confinement frequency in the y-direction. Thus, the influence of the magnetic field strength is contained within ω_c.

The term $|e|F(x+y)$ [cf. Eqn (1)] represents the contribution coming from the static electric field of magnitude F and operating along the x and y axes.

The function $\xi(x,y)$ [cf. (eqn(1)] possesses the features of zero-mean and spatial δ correlation and represents Gaussian white noise. $g(x,y)$ is another function connected with $\xi(x,y)$, that mathematically describes the above features as given below:

$$\langle g(x,y)\rangle = 0 \quad (4)$$

and

$$\langle g(x,y)g(x',y')\rangle = 2\zeta\delta[(x,y)-(x',y')] \quad (5)$$

respectively, with noise strength ζ. Box-Muller algorithm ensures that $g(x,y)$ follows a Gaussian distribution. The type of connection between $\xi(x,y)$ and $g(x,y)$ defines two different ways of introducing Gaussian white noise to the QD, viz. additive white noise and multiplicative white noise given by

$$\xi(x,y) = \lambda_1 g(x,y), \text{for additive white noise (NSWH1)} \quad (6)$$

and

$$\xi(x,y) = \lambda_2 g(x,y)(x+y), \text{for multiplicative white noise (NSWH2)} \quad (7)$$

λ_1 and λ_2 are the two constants.

The linear variational principle has now been invoked to approximate a solution to the time-independent Schrodinger equation. For this purpose, the ordinary product of the harmonic oscillator eigenfunctions has been chosen as the basis function $\psi_k(x,y)$. The normalized eigenvectors and the energy eigenvalues can thus be subsequently generated.

The ISTE between the states $|0\rangle$ and $|j\rangle$ is given by [47,48,54]

$$E_{sub,0j}^{trans} = E_{sub,j} - E_{sub,0} \quad (8)$$

and the NISTE is given by [47,54]

$$NE_{sub,0j}^{trans} = E_{sub,0j}^{trans}/E_{sub,0} = \left(E_{sub,j} - E_{sub,0}\right)/E_{sub,0} \quad (9)$$

3. Results and Discussion

In general, for the *GaAs* QD, we have chosen the following values for various physical quantities: $m^* = 0.067m_0$, where m_0 is the vacuum electron mass, $\hbar\omega_0 = 100.0$ meV, $F = 100$ kV/cm, $B = 5.0$ T, $P = 50$ kbar, $T = 100$ K, $x = 0.5$ and $\zeta = 1.0\times10^{-4}$, respectively.

3.1. Effect of various physical parameters on ISTE and NISTE.

Figure 1(a) and Figure 1(b) depict the plots of ISTE and NISTE, respectively, as a function of the electric field (F), including and excluding noise. Without noise and in the presence of NSWH1, it is observed that both ISTE and NISTE undergo steady enhancement with an increase in F. However, the enhancement appears more prominent and nonlinear for NISTE than ISTE. In the presence of NSWH2, however, the ISTE and NISTE plots depict maximization around F ~ 64 kV/cm and F ~ 31 kV/cm, respectively. It can be noted that the maximum appearing in the NISTE plot is much more prominent than that of the ISTE plot. Furthermore, over the whole range of the electric field, applied NSWH1 (NSWH2) lowers (raises) ISTE with respect to the state free of noise. On the other hand, for NISTE, the above magnitude sequence is found up to F ~ 56 kV/cm. Within the range F ~ 56 kV/cm to F ~ 62 kV/cm, NISTE exhibits the highest magnitude in the absence of noise, followed by that in the presence of NSWH2 and the presence of NSWH1. Beyond F ~ 62 kV/cm, a further change in the magnitude sequence is found when NISTE continues to attain maximum value without noise, followed by that in the presence of NSWH1 and the presence of NSWH2. Thus, NISTE shows greater responsiveness and delicacy towards the change in the strength of the electric field than ISTE.

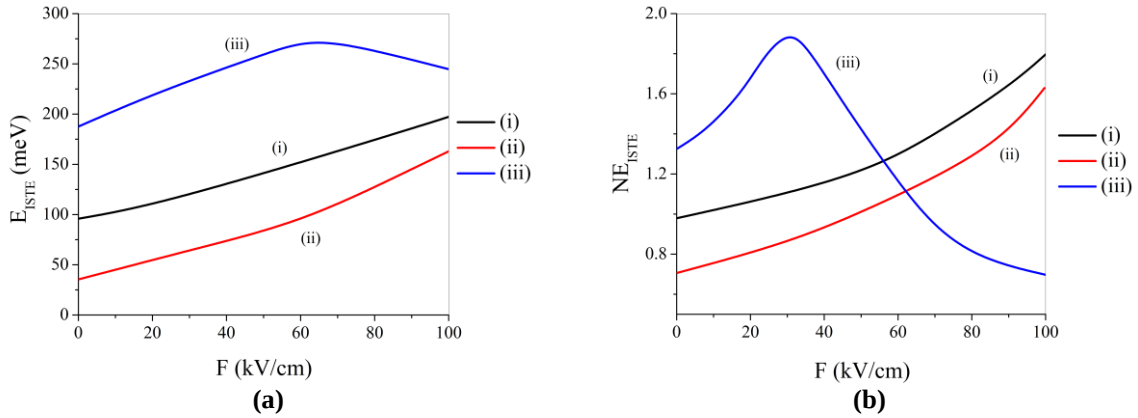

(a) **(b)**

Figure 1. Plots of **(a)** ISTE; **(b)** NISTE against the electric field: **(i)** without noise, **(ii)** in the presence of NSWH1, and **(iii)** in the presence of NSWH2.

Figure 2(a) and Figure 2(b) delineate the profiles of ISTE and NISTE, respectively, with the variation of magnetic field (B), with and without noise. Safwan *et al*. explored the effect of a magnetic field on ISTE in inverse parabolic QD [44]. Deyasi *et al*. have inspected the influence of magnetic fields on the ISTE of circular QDs [51]. ISTE and NISTE display a steady nonlinear decreasing trend with an increase in the magnetic field strength, with and without noise. Increasing the magnetic field strength introduces additional confinement, which enhances the energy eigenvalues. However, if the ground state energy is more enhanced than the excited state energy, the difference will be small. This is reflected by a drop in ISTE as the magnetic field increases. It can be further noted that the said decreasing trend is much more pronounced in the NISTE plots than in the ISTE plots. Thus, NISTE reveals a larger sensitivity towards the alteration in the magnetic field strength than ISTE. Moreover, applied NSWH1 (NSWH2) diminishes (enhances) both ISTE and NISTE with respect to the noise-free condition.

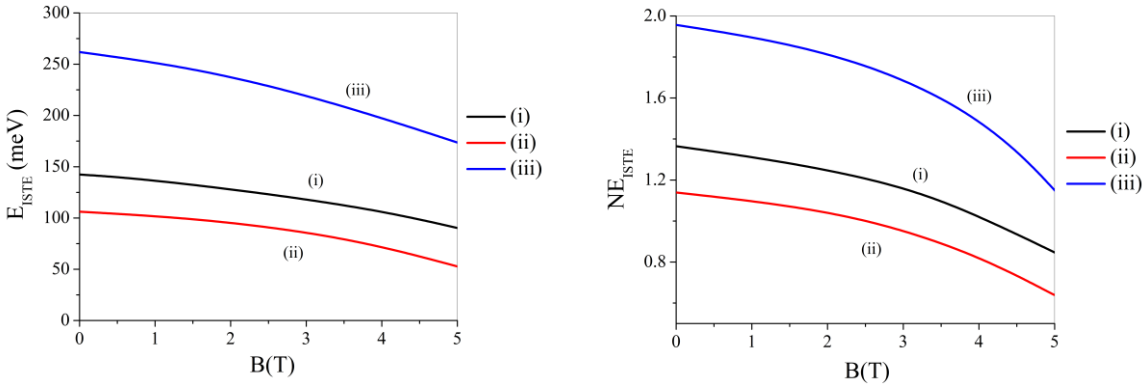

(a) **(b)**

Figure 2. Plots of **(a)** ISTE; **(b)** NISTE as a function of magnetic field: **(i)** absence of noise, **(ii)** under NSWH1 and **(iii)** under NSWH2.

Figure 3(a) and Figure 3(b) depict the ISTE and NISTE curves, respectively, following the change of confinement energy ($\hbar\omega_0$), in the presence and absence of noise. Safwan *et al*. explored the effect of confinement on ISTE in inverse parabolic QD [44]. Nasrallah *et al*. examined the confinement effect on ISTE for CdS/SiO_2 QDs [43]. Mese has enquired about the influence of confinement potential on ISTE and NISTE for GaAs/$Ga_{1-x}Al_xAs$ spherical QD [47]. Deyasi *et al*. have inspected the influence of confinement on ISTE of circular QDs [51]. Mese *et al*. also studied the confinement effect on ISTE for spherical QDs made up of different materials [54]. Regardless of the presence of noise, both ISTE and NISTE reveal monotonic enhancement with the increase in the confinement energy [43,44,47,51,54] due to a change in

the electronic probability density [47]. On all occasions, the enhancement appears to be nonlinear. However, the NISTE plots exhibit much more prominent nonlinearity only in the presence of NSWH2 with respect to other conditions. It can be observed that, in the absence of NSWH2, the various curves approach each other at low confinement. Similar to the previous observations, the presence of NSWH1 (NSWH2) reduces (augments) ISTE compared to the noise-free condition. However, the situation becomes a little bit more complex for NISTE. In this case, the sequence of magnitude of NISTE in the presence and absence of noise depends on the range of magnitude of the confinement energy. Now, up to a confinement energy of ~ 166 meV, NISTE exhibits maximum value without noise, sequentially followed by those in the presence of NSWH1 and NSWH2. Inside the confinement range of ~166 to ~ 213 meV, NISTE continues registering the highest values without noise. However, sequentially followed by those in the presence of NSWH2 and NSWH1. Beyond the confinement strength of ~ 213 meV, the presence of NSWH1 (NSWH2) reduces (augments) NISTE compared to the noise-free condition. Thus, NISTE curves give more information than ISTE about the role of the confinement potential due to their greater sensitivity to the confinement strength [47].

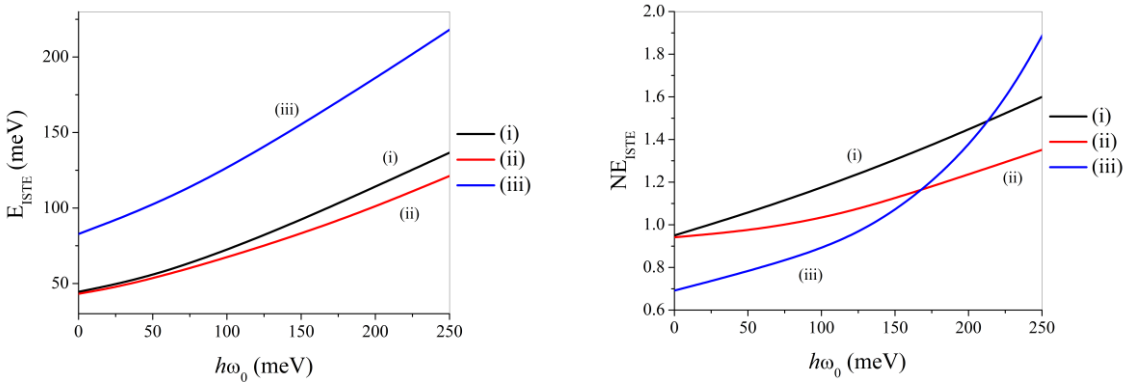

(a) **(b)**

Figure 3. (a) ISTE; **(b)** NISTE diagrams with the change of confinement energy: **(i)** devoid of noise, **(ii)** with NSWH1 and **(iii)** with NSWH2.

Figure 4(a) and Figure 4(b) display the ISTE and NISTE curves, respectively, with a variation of the aluminum concentration (x) in the presence and absence of noise. For this purpose, we have envisaged $Al_xGa_{1-x}As$ alloy QD, whose effective mass is given by $m^* = (0.067 + 0.083x)m_0$ [36]. Mese investigated the role of x on ISTE and NISTE for $GaAs/Ga_{1-x}Al_xAs$ spherical QD [47]. Without noise and in the presence of NSWH1, it is observed that both ISTE and NISTE undergo steady enhancement with an increase in x [47]. The enhancement occurs due to the enhancement of confinement associated with increased aluminum concentration. However, the enhancement appears more prominent and nonlinear for NISTE than ISTE. In the presence of NSWH2, however, although the ISTE shows a steady increase with x, NISTE plots depict noticeable maximization around x ~ 0.45. Furthermore, over the whole range of x, applied NSWH1 (NSWH2) lowers (raises) ISTE with respect to the state free of noise. On the other hand, for NISTE, the above magnitude sequence is found up to x ~ 0.6. Within the narrow range of x ~ 0.6 to x ~ 0.63, NISTE exhibits the highest magnitude in the absence of noise, followed by that in the presence of NSWH2 and the presence of NSWH1. Beyond x ~ 0.63, a further change in the magnitude sequence is found when NISTE continues to attain maximum value without noise, followed by that in the presence of NSWH1 and the presence of NSWH2. Thus, NISTE shows greater sensitivity and subtlety towards the change in aluminum concentration than ISTE.

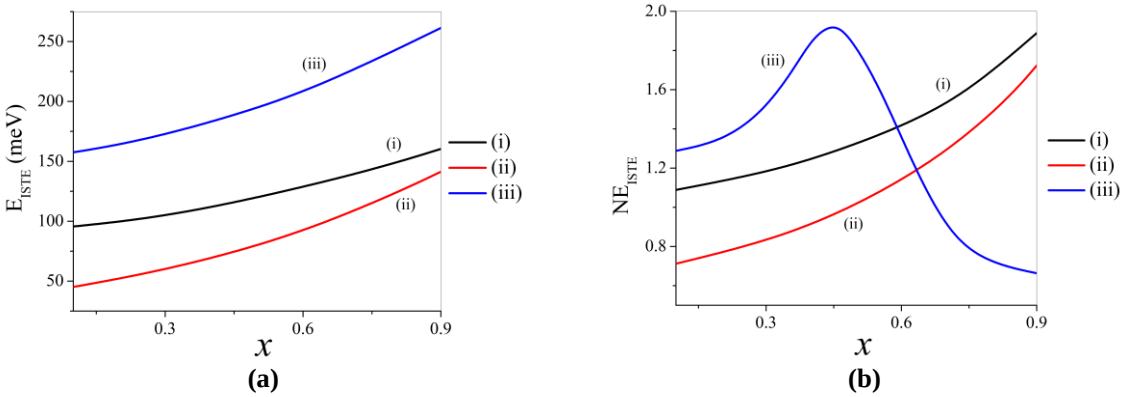

(a) **(b)**

Figure 4. (a) ISTE; **(b)** NISTE diagrams against the variation of aluminum concentration: **(i)** devoid of noise, **(ii)** under applied NSWH1, and **(iii)** under applied NSWH2.

The *anisotropy parameter*, η, stands as the reflector of the geometrical anisotropy of the system and reads [55–58] $\eta = \frac{\Omega}{\omega_0}$ [cf. eqn(3)]. Figure 5(a) and Figure 5(b) evince the ISTE and NISTE plots, respectively, pursuing the change of including and excluding noise. Only in the absence of noise do the ISTE and NISTE plots reveal a similar pattern as η increases. In this case, both ISTE and NISTE regularly fall in a nonlinear way with an increase in η. However, the extent of nonlinearity and the sharpness of fall are much more noticeable for NISTE than ISTE. The ISTE and NISTE profiles manifest distinctly different features in the presence of noise. NISTE reveals a steady decline with η even in the presence of noise (both NSWH1 and NSWH2). However, under NSWH1, the ISTE plots initially increase with η and culminate in saturation at large η, reflecting the independence of ISTE on the anisotropy. On the other hand, under NSWH2, the ISTE plot exhibits minimization in the vicinity of $\eta \sim 4$. Here, NSWH1 and NSWH2 were also applied to lower and raise the ISTE and NISTE, respectively, compared with the noise-free condition.

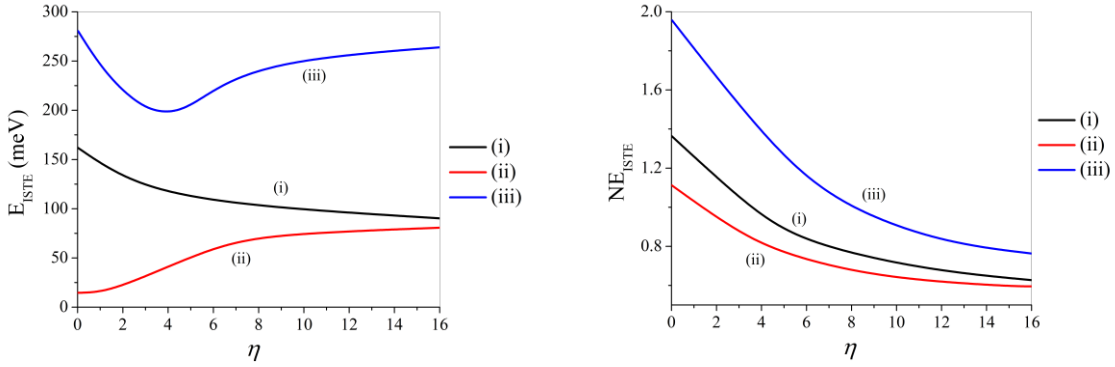

(a) **(b)**

Figure 5. (a) ISTE; **(b)** NISTE diagrams against the variation of anisotropy parameter: **(i)** noise-free atmosphere, **(ii)** presence of NSWH1, and **(iii)** presence of NSWH2.

Figure 6(a) and Figure 6(b) unveil the ISTE and NISTE profiles, respectively, against hydrostatic pressure (P), with and without noise. In this case, one needs to consider the pressure-dependent effective mass given by $m^*(P)=m^*(0)\exp(0.078P)$ (P in kbar) [59]. In the absence of noise and under NSWH1, both ISTE and NISTE plots display a monotonic rise with increased pressure. Such behavior indicates the imposition of additional confinement with an increase in pressure. However, for NISTE, the said rise appears to be much more nonlinear and conspicuous than that of ISTE. In the presence of NSWH2, the ISTE and NISTE plots exhibit huge qualitative differences. Now, whereas the ISTE undergoes a modest nonlinear rise with the increase in pressure, the NISTE reveals a profound minimization in the proximity of $P \sim$

86 kbar. Furthermore, applied NSWH1 and NSWH2 shrink and enhance the ISTE, respectively, compared to the state where no noise effect can be realized. However, the situation becomes more complex for NISTE. In this case, the sequence of magnitude of NISTE in the presence and absence of noise depends on the range of magnitude of the hydrostatic pressure. Now, up to $P \sim 55$ kbar, NISTE exhibits maximum value under NSWH2, sequentially followed by those without noise and in the presence of NSWH1. Inside the pressure range of $P \sim 55$ kbar to $P \sim 68$ kbar, NISTE exhibits the largest value under noise-free conditions, sequentially followed by that under NSWH2 and NSWH1. Next, within the pressure regime of $P \sim 68$ kbar to $P \sim 105$ kbar, NISTE exhibits the highest value under noise-free conditions, sequentially followed by that under NSWH1 and NSWH2. Inside the pressure range of $P \sim 105$ kbar to $P \sim 121$ kbar, NISTE reveals the same sequence of magnitude in the presence and absence of noise as previously observed inside the pressure range of $P \sim 55$ kbar to $P \sim 68$kbar. As pressure exceeds the value of 121 kbar, NISTE continues to register maximum values under applied NSWH2, sequentially followed by that without noise and under NSWH1. All these observations indicate considerable superiority of the NISTE curves over the corresponding ISTE curves in realizing the finer intricacies of the effect of hydrostatic pressure.

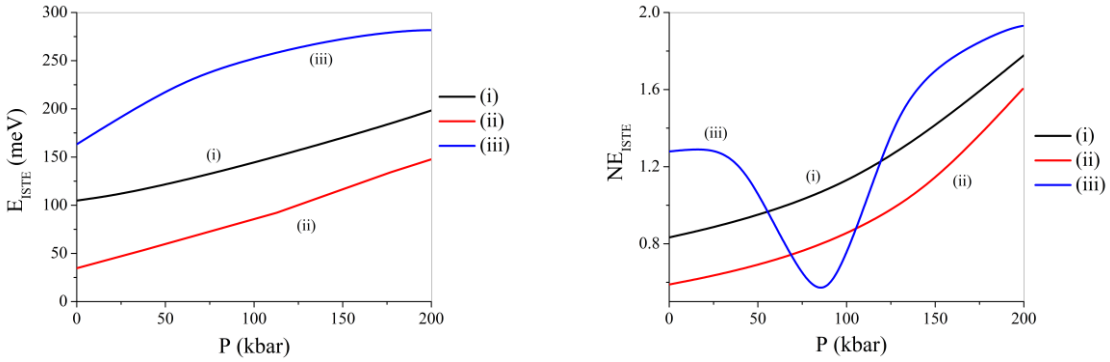

(a) **(b)**

Figure 6. (a) ISTE; **(b)** NISTE profiles plotted against the hydrostatic pressure: **(i)** without considering noise, **(ii)** considering NSWH1, and **(iii)** considering NSWH2.

Figure 7(a) and Figure 7(b) describe the ISTE and NISTE curves, respectively, with progressive alteration of temperature (T) in the presence and absence of noise. In this case, one needs to consider the pressure and temperature-dependent effective mass for *GaAs* given in the work of Lu *et al*. [60]. Mese examined the effect of temperature on ISTE and NISTE of $GaAs/Ga_{1-x}Al_xAs$ spherical QD [47]. Without noise and in the presence of NSWH1, it is observed that both ISTE and NISTE undergo steady enhancement with an increase in temperature. An increase in temperature generally reduces the confinement effect, leading to a drop in the energy eigenvalues [47]. However, if the drop in the ground state energy becomes greater than the drop in the excited state energy, the ISTE will increase overall. The above enhancement appears more prominent and nonlinear for NISTE than ISTE. In the presence of NSWH2, however, although the ISTE shows a steady increase with temperature, NISTE plots depict noticeable maximization around $T \sim 105$ K. Furthermore, over the whole temperature range, applied NSWH1 (NSWH2) lowers (raises) ISTE with respect to the state free of noise.

On the other hand, for NISTE, the above sequence of magnitude is found up to $T \sim 160$ K. Within the range $T \sim 160$ K to $T \sim 183$ K, NISTE exhibits the highest magnitude in the absence of noise, followed by that in the presence of NSWH2 and the presence of NSWH1. Beyond $T \sim 183$ K, a further change in the magnitude sequence is found when NISTE continues to attain the highest value without noise, followed by that in the presence of NSWH1 and in

the presence of NSWH2. Thus, NISTE provides much finer information about the influence of temperature than ISTE.

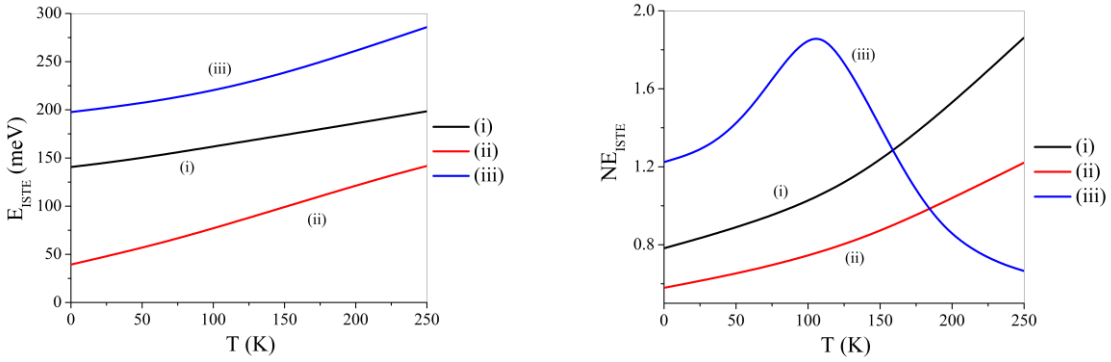

(a) **(b)**

Figure 7. (a) ISTE; **(b)** NISTE curves depicted against temperature: **(i)** noise-free condition, **(ii)** under applied NSWH1, and **(iii)** under applied NSWH2.

We now enquire about the impact of noise strength on ISTE and NISTE. Figure 8(a) and Figure 8(b) uncover the ISTE and NISTE diagrams, respectively, when noise strength (ζ) varies over a range, both for NSWH1 and NSWH2. In the presence of NSWH1 (NSWH2), both ISTE and NISTE have been found to decrease (increase) steadily with an increase in the noise strength in a nonlinear way. The rate of increase/decrease has been found to be much more prominent for NISTE than ISTE. Additionally, the interval between the lines corresponding to NSWH1 and NSWH2 comes out to be much more broad for NISTE than for ISTE. Moreover, under all conditions, the interval between the two lines continually reduces with a fall in noise strength, and the ISTE and NISTE approach their respective noise-free values in the limit of vanishingly small noise strength. Again, the approach towards the noise-free value has been much sharper for NISTE than ISTE. These observations clearly announce the greater utility of NISTE plots in analyzing the role of noise strength than the ISTE plots. In addition, over the entire range of the noise strength, the introduction of NSWH1 (NSWH2) diminishes (enhances) both ISTE and NISTE compared to the noise-free ambiance.

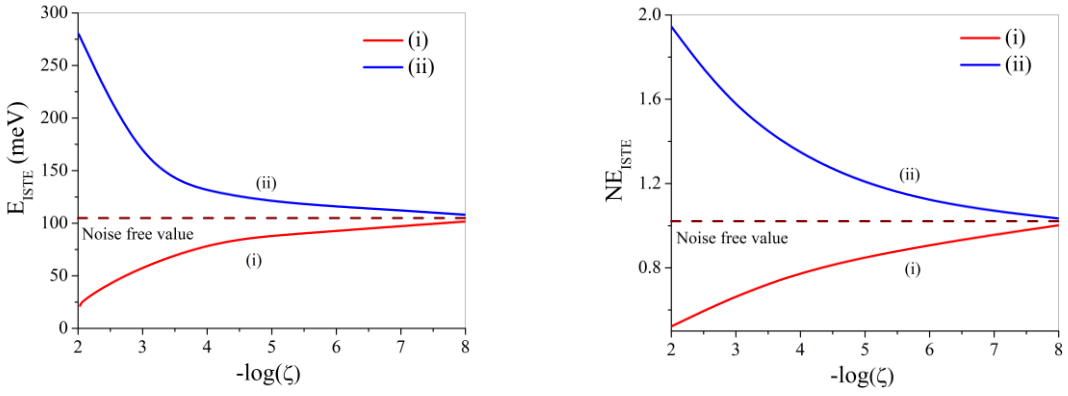

(a) **(b)**

Figure 8. (a) ISTE; **(b)** NISTE plotted against the negative logarithm of noise strength: **(i)** for applied NSWH1 and **(ii)** for applied NSWH2.

Finally, we study the ISTE and NISTE profiles in the presence of anharmonicities in the confinement potential. For this purpose, we introduce another term, V_{anh}, in the QD Hamiltonian [cf. eqn(1)]. We have considered anharmonic contributions of odd and even parties, based on which V_{anh} can be written as

$$V_{anh} = k(x^3 + y^3), \text{ the odd anharmonic potential} \quad (10)$$

and

$$V_{anh} = k(x^4 + y^4), \quad \text{the even anharmonic potential} \quad (11)$$

k being the anharmonicity constant.

Figure 9(a) and Figure 9(b) discern the ISTE and NISTE profiles, respectively, as a function of the negative logarithm of anharmonicity constant, considering and ignoring the noise and in the presence of both types of anharmonicities. In the presence of odd anharmonicity, the ISTE curves exhibit moderate decline (increase) in a nonlinear manner with an increase in the anharmonicity constant without noise and under NSWH2 (NSWH1). The NISTE plots, on the other hand, depict steady nonlinear growth (fall) in the presence (absence) of noise with an increase in the anharmonicity constant. The prominence of growth/fall and the nonlinearity of the NISTE plots are much greater than those of the corresponding ISTE plots. It can be further noted that, over the entire range of *k*, applied NSWH1 (NSWH2) lowers (raises) the ISTE with respect to the condition free of noise. The scenario becomes a little bit more delicate for NISTE. Now, NISTE exhibits the largest magnitude over the whole range of *k* in the presence of NSWH2. The relative magnitude of NISTE in the absence of noise and the presence of NSWH1 undergoes a changeover in the vicinity of $k \sim 10^{-4}$. Whereas in the regime $k < 10^{-4}$, NISTE shows higher values in the absence of noise than in the presence of NSWH1, the situation reverses as soon as *k* exceeds the value of $\sim 10^{-4}$.

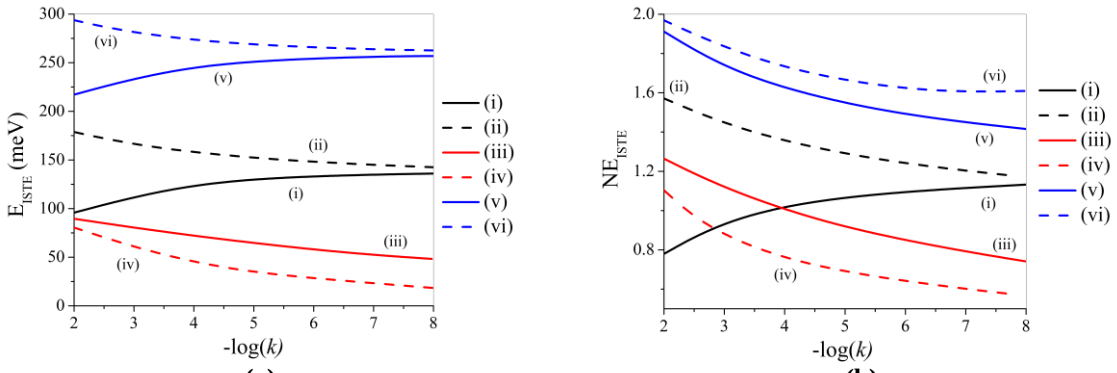

Figure 9. (a) ISTE; **(b)** NISTE plotted against negative of logarithm of anharmonicity constant: **(i)** absence of noise and odd anharmonicity, **(ii)** without noise and even anharmonicity, **(iii)** NSWH1 and odd anharmonicity, **(iv)** NSWH1 and even anharmonicity, **(v)** NSWH2 and odd anharmonicity and **(vi)** NSWH2 and even anharmonicity.

In the presence of even anharmonicity, regardless of the presence of noise, both ISTE and NISTE reveal modest growth with an increase in the anharmonicity constant. The growth takes place in a nonlinear way, with a much greater extent of nonlinearity for NISTE than for ISTE. Moreover, both ISTE and NISTE applied NSWH1 (NSWH2) to enhance (deplete) their magnitudes compared with the condition without any noise effect. It, therefore, comes out that, both in the presence of odd and even anharmonicities, the NISTE plots appear to be much superior to the ISTE plots in unveiling the influence of anharmonicity.

3.2. General remarks.

The behavior of ISTE and NISTE with the variation of different physical quantities is extremely case-sensitive. It delicately depends on the interplay between the particular physical parameter considered and the application of noise (including its way of application, i.e., NSWH1 or NSWH2). The introduction of noise modifies the QD confinement potential, thereby affecting the ISTE and NISTE. The mode of entry of noise also plays a vital role since NSWH1 and NSWH2 couple with QD in different ways and modify the QD confinement

diversely. This happens because NSWH1 adds to the QD Hamiltonian, while NSWH2 couples with the QD coordinates. Thus, most often, NSWH2 modifies the QD confinement much more than NSWH1, bringing about greater deviation of ISTE and NISTE profiles from that under the noise-free condition.

It has been found that, on most occasions, NISTE can highlight the effects of various physical parameters much more prominently and delicately than ISTE. These effects are revealed through the rate of enhancement/decline, the extent of nonlinearity, the prominence of maximization/minimization, and relative magnitudes without noise and in the presence of NSWH1/NSWH2. It has also been observed that, depending on the presence/absence of noise and the mode of entrance of noise, ISTE and NISTE can exhibit steady growth, steady fall, and maximization/minimization (in the vicinity of certain values of the physical quantities). The appearance of the above features depends on how the energy separation between the ground state and the excited state varies with respect to the variation of various physical parameters. A steady increase in the magnitude of physical quantities (depending on their nature) can either increase or decrease the system's confinement. An increase (decrease) in the confinement raises (lowers) the energies of the eigenstates. However, depending on the relative change in the magnitudes of the ground state and the excited state energies, their separation may either enhance steadily or diminish steadily or can maximize or minimize (in the neighborhood of certain values of the physical parameters), thus, justifying the features of the ISTE plots.

4. Conclusions

The ISTE and NISTE of *GaAs* QD have been meticulously investigated under the influence of Gaussian white noise. Two different modes of inclusion of noise viz. NSWH1 and NSWH2 have been envisaged. The study reveals that, depending on the presence/absence of noise and its mode, ISTE and NISTE (when monitored against the change of different physical parameters) exhibit steady growth, steady fall, maximization, and minimization. The findings can be summarized as follows: Both ISTE and NISTE steadily increase under all conditions with an increase in the confinement strength; Both ISTE and NISTE steadily decrease under all conditions with an increase in the magnetic field strength; Only in the absence of noise and in the presence of additive noise do ISTE and NISTE steadily grow with the increase in electric field strength, aluminum concentration, pressure, and temperature; In the presence of multiplicative noise, ISTE steadily enhances with an increase in aluminum concentration, pressure, and temperature. However, when an electric field is varied, ISTE undergoes maximization around F ~ 64 kV/cm. Under identical conditions, NISTE displays maximization around F ~ 31 kV/cm (during the variation of the electric field), x ~ 0.45 (during the variation of aluminum concentration), T ~ 160 K (during the temperature variation), and minimization around P ~ 86 kbar (during the variation of hydrostatic pressure); With the increase in the anisotropy of the system, the ISTE decreases in the absence of noise, increases in the presence of additive noise, and minimizes around η ~ 4 in the presence of multiplicative noise. However, NISTE monotonically diminishes with an increase in anisotropy under all conditions; Presence of additive (multiplicative) noise depletes (augments) ISTE with respect to the noise-free environment during the variation of the electric field, magnetic field, confinement potential, aluminum concentration, anisotropy, hydrostatic pressure, and temperature. NISTE exhibits a similar sequence during the variation of magnetic field and anisotropy. However, the sequence of the magnitude of NISTE in the presence and absence of noise, taking into account the noise mode, reveals complex dependence on the range of magnitude of the given physical parameter

concerned during the change of electric field strength, confinement strength, aluminum concentration, hydrostatic pressure, and temperature; With the increase in the noise strength, both ISTE and NISTE delineate regular fall (growth) under applied NSWH1 (NSWH2); In the presence of anharmonicity in the QD confinement potential, the ISTE and NISTE profiles are also governed by the strength and the parity/symmetry of the anharmonic potential.

Throughout the entire study, the NISTE plots have proven superior to the ISTE plots in realizing the influences of various physical parameters. The NISTE plots unveil a greater rate of enhancement/decline, more nonlinearity, sharper maximization/minimization, and more subtlety in their relative magnitude with and without noise.

These findings are expected to be considerably relevant in understanding the optical properties of low-dimensional nanostructures under the presence of noise and anharmonicity in the confinement potential.

Funding

This research received no external funding.

Acknowledgments

The authors, B.B. and M.G., thank DST-FIST (Govt. of India) and UGC-SAP (Govt. of India) for support.

Conflicts of Interest

The authors declare no conflict of interest.

References

1. Duque, C.A.; Porras-Montenegro, N.; Barticevic, Z.; Pacheco, M.; Oliveira, L. E. Electron-hole transitions in self-assembled *InAs*/*GaAs* quantum dots: Effects of applied magnetic fields and hydrostatic pressure. *Microelectronics J.* **2005**, *36*, 231-233, https://doi.org/10.1016/j.mejo.2005.04.001.
2. Al, E.B.; Kasapoglu, E.; Sakiroglu, S.; Sari, H.; Sökmen, I.; Duque, C.A. Binding energies and optical absorption of donor impurities in spherical quantum dot under applied magnetic field. *Physica E* **2020**, *119*, 114011, https://doi.org/10.1016/j.physe.2020.114011.
3. Barseghyan, M.G.; Manaselyan, A.; Kirakosyan, A.A.; Pérez, L.M.; Laroze, D. Effective tuning of isotropic and anisotropic properties of quantum dots and rings by external fields. *Physica E* **2020**, *117*, 113807, https://doi.org/10.1016/j.physe.2019.113807.
4. Niculescu, E.C. 1*s*-2*p*± transitions between hydrogenic states in *GaAs* low-dimensional systems under external fields. *Superlattices and Microstructures* **2001**, *29*, 385-393, https://doi.org/10.1006/spmi.2001.0985.
5. Kirak, M.; Altinok, Y.; Yilmaz, S. The effects of the hydrostatic pressure and temperature on binding energy and optical properties of a donor impurity in a spherical quantum dot under external electric field. *J. Lumin.* **2013**, *136*, 415-421, https://doi.org/10.1016/j.jlumin.2012.12.026.
6. Villamil, P.; Porras-Montenegro, N.; Granada, J.C. Infrared transitions between hydrogenic states in cylindrical *GaAs* quantum-well wires under applied magnetic fields. *Phys. Rev. B* **1999**, *59*, 1605-1608, https://doi.org/10.1103/PhysRevB.59.1605.
7. Başer, P.; Altuntas, I.; Elagoz, S. The hydrostatic pressure and temperature effects on hydrogenic impurity binding energies in *GaAs*/$In_xGa_{1-x}As$/*GaAs* square quantum well. *Superlattices and Microstructures* **2016**, *92*, 210-216, https://doi.org/10.1016/j.spmi.2015.12.010.
8. Sivakami, A.; Gayathri, V. Hydrostatic pressure and temperature dependence of dielectric mismatch effect on the impurity binding energy in a spherical quantum dot. *Superlattices and Microstructures* **2013**, *58*, 218-227, https://doi.org/10.1016/j.spmi.2013.03.002.

9. Yakar, Y.; Çakır, B.; Demir, C.; Özmen, A. Coulomb, exchange, kinetic, nuclear attraction and ionization energies of two-electron quantum dot with finite confinement potential. *Phys. Lett. A* **2023**, *466*, 128724, https://doi.org/10.1016/j.physleta.2023.128724.
10. Özmen, A.; Yakar, Y.; Çakir, B.; Atav, Ü. Computation of the oscillator strength and absorption coefficients for the intersubband transitions of the spherical quantum dot. *Optics Commun.* **2009**, *282*, 3999-4004, https://doi.org/10.1016/j.optcom.2009.06.043.
11. Vaseghi, B.; Sadri, M.; Rezaei, G.; Gharaati, A. Optical rectification and third harmonic generation of spherical quantum dots: Controlling via external factors. *Physica B* **2015**, *457*, 212-217, https://doi.org/10.1016/j.physb.2014.10.020.
12. Bahar, M.K.; Başer, P. Nonlinear optical characteristics of thermodynamic effects-and electric field-triggered Mathieu quantum dot. *Micro and Nanostructures* **2022**, *170*, 207371, https://doi.org/10.1016/j.micrna.2022.207371.
13. Tuzemen, A.T.; Dakhlaoui, H.; Ungan, F. Effects of hydrostatic pressure and temperature on the nonlinear optical properties of *GaAs*/*GaAlAs* zigzag quantum well. *Philosophical Magazine* **2022**, *102*, 2428-2443, https://doi.org/10.1080/14786435.2022.2111028.
14. Makhlouf, D.; Choubani, M.; Saidi, F.; Maaref, H. Applied electric and magnetic fields effects on the nonlinear optical rectification and the carriers transition lifetime in *InAs*/*GaAs* core/shell quantum dot. *Mater. Chem. Phys.* **2021**, *267*, 124660, https://doi.org/10.1016/j.matchemphys.2021.124660.
15. Ghajarpour-Nobandegani, S.; Ashra-Dalkhani, V.; Karimi, M.J. Effects of external fields on the optical absorption of quantum multirings. *Int. J. Mod. Phys. B* **2020**, *34*, 2050153, https://doi.org/10.1142/S0217979220501532.
16. Ghajarpour-Nobandegani, S.; Karimi, M.J. Effects of hydrogenic impurity and external fields on the optical absorption of ring-shaped elliptical quantum dot. *Optical Materials* **2018**, *82*, 75-80, https://doi.org/10.1016/j.optmat.2018.05.045.
17. Hayrapetyan, D.B.; Baghdasaryan, D.A.; Kazaryan, E.M.; Pokutnyi, S.I.; Sarkisyan, H.A. Exciton states and optical absorption in core/shell/shell spherical quantum dot. *Chem. Phys.* **2018**, *506*, 26-30, https://doi.org/10.1016/j.chemphys.2018.03.025.
18. Rodríguez-Magdaleno, K.A.; Nava-Maldonado, F.M.; Kasapoglu, E.; Mora-Ramos, M.E.; Ungan, F.; Martínez-Orozco, J.C. Nonlinear absorption coefficient and relative refractive index change for Konwent potential quantum well as a function of intense laser field effect. *Physica E* **2023**, *148*, 115618, https://doi.org/10.1016/j.physe.2022.115618.
19. Haghighatzadeh, A.; Attarzadeh, A.; Durmuslar, A.S.; Al, E.B.; Ungan, F. Modeling of electronic spectra and optical responses of a semiconductor *AlGaAs*/*GaAs* quantum well with three-step barriers: the role of external perturbations and impurity. *Eur. Phys. J. Plus* **2024**, *139*, 353, https://doi.org/10.1140/epjp/s13360-024-05165-4.
20. El-Yadri, Md.; El Hamdaoui, J.; Aghoutane, N.; Pérez, L.M.; Baskoutas, S.; Laroze, D.; Díaz, P.; Feddi, El M. Optoelectronic properties of a cylindrical core/shell nanowire: Effect of quantum confinement and magnetic field. *Nanomaterials* **2023**, *13*, 1334, https://doi.org/10.3390/nano13081334.
21. Sayrac, M.; Dakhlaoui, H.; Mora-Ramos, M.E.; Ungan, F. Hydrostatic pressure and temperature effects on nonlinear optical properties in Harmonic-Gaussian asymmetric double quantum wells. *Physica Scripta* **2024**, *99*, 045942, https://doi.org/10.1088/1402-4896/ad3150.
22. Mughnetsyan, V.N.; Manaselyan, A. Kh.; Barseghyan, M.G.; Kirakosyan, A.A. Simultaneous effects of hydrostatic pressure and spin-orbit coupling on linear and nonlinear intraband optical absorption coefficients in a *GaAs* quantum ring. *J. Lumin.* **2013**, *134*, 24-27, https://doi.org/10.1016/j.jlumin.2012.09.023.
23. A. Boda, A.; Chatterjee, A. Transition energies and magnetic properties of a neutral donor complex in a Gaussian *GaAs* quantum dot. *Superlattices and Microstructures* **2016**, *97*, 268-276, https://doi.org/10.1016/j.spmi.2016.06.009.
24. de Almeida, R.B.; Borgesa, A.N.; Machado, P.C. M.; Osorio, F. A.P. Confinement effect on the intradonor 1*s*-2*p*+ transition energies in *GaN* quantum wells. *Microelectronic J.* **2005**, *36*, 431-433, https://doi.org/10.1016/j.mejo.2005.02.039.
25. Mikhail, I. F.I.; Ismail, I.M.M. Hydrogenic impurity in a quantum dot: comparison between the variational and strong perturbation methods. *Superlattices and Microstructures* **2010**, *48*, 388-400, https://doi.org/10.1016/j.spmi.2010.08.004.

26. Kachu, A.; Boda, A. Confinement shape effects on binding energy, transition energy, and oscillator strength of a D^0 impurity in a quantum dot in the presence of spin-orbit interactions. *Physica E* **2024**, *155*, 115826, https://doi.org/10.1016/j.physe.2023.115826.
27. Mantashian, G.A.; Zaqaryan, N.A.; Mantashyan, P.A.; Sarkisyan, H.A.; Baskoutas, S.; Hayrapetyan, D.B. Linear and nonlinear optical absorption of *CdSe*/*CdS* core/shell quantum dots in the presence of donor impurity. *Atoms* **2021**, *9*, 75, https://doi.org/10.3390/atoms9040075.
28. Zeng, Z.; Garoufalis, C.S.; Terzis, A.F.; Baskoutas, S. Linear and nonlinear optical properties of ZnO/ZnS and ZnS/ZnO core shell quantum dots: Effects of shell thickness, impurity, and dielectric environment *J. Appl. Phys.* **2013**, *114*, 023510, https://doi.org/10.1063/1.4813094.
29. Duque, C.A.; Mora-Ramos, M.E.; Kasapoglu, E.; Ungan, F.; Yesilgul, U.; Sakiroglu, S.; Sari, H.; Sökmen, I. Impurity-related linear and nonlinear optical response in quantum-well wires with triangular cross section. *J. Lumin.* **2013**, *143*, 304-313, https://doi.org/10.1016/j.jlumin.2013.04.048.
30. Khordad, R.; Bahramiyan, H. Impurity position effect on optical properties of various quantum dots. *Physica E* **2015**, *66*, 107-115, https://doi.org/10.1016/j.physe.2014.09.021.
31. Bahramiyan, H.; Khordad, R. Effect of various factors on binding energy of pyramid quantum dot: pressure, temperature and impurity position. *Optical and Quantum Electronics* **2014**, *46*, 719-729, https://doi.org/10.1007/s11082-013-9782-1.
32. Niculescu, E.C.; Stan, C.; Bejan, D.; Cartoaje, C. Impurity and eccentricity effects on the nonlinear optical rectification in a quantum ring under lateral electric fields. *J. Appl. Phys.* **2017**, *122*, 144301, https://doi.org/10.1063/1.4999673.
33. Bejan, D.; Stan, C. Impurity and geometry effects on the optical rectification spectra of quasi-elliptical double quantum rings. *Physica E* **2023**, *147*, 115598, https://doi.org/10.1016/j.physe.2022.115598.
34. Ghazi, H.El.; Jorio, A.; Zorkani, I. Theoretical investigation of stark effect on shallow donor binding energy in *InGaN* spherical QD-QW. *Physica B* **2013**, *422*, 47-50, https://doi.org/10.1016/j.physb.2013.04.011.
35. Kirak, M.; Yilmaz, S.; Şahin, M.; Gencaslan, M. The electric field effects on the binding energies and the nonlinear optical properties of a donor impurity in a spherical quantum dot. *J. Appl. Phys.* **2011**, *109*, 094309, https://doi.org/10.1063/1.3582137.
36. Rezaei, G.; Vahdani, M.R.K.; Vaseghi, B. Nonlinear optical properties of a hydrogenic impurity in an ellipsoidal finite potential quantum dot. *Current Appl. Phys.* **2011**, *11*, 176-181, https://doi.org/10.1016/j.cap.2010.07.002.
37. Filipović, N.; Stevanović, L.; Pavlović, V. Light storage and retrieval in spherical semiconductor quantum dots with on-center hydrogen impurity in magnetic field. *Superlattices and Microstructures* **2020**, *147*, 106691, https://doi.org/10.1016/j.spmi.2020.106691.
38. Solaimani, M. Stark shift of binding energy for on and off-center donor impurities in quantum rings under the influence of charged rods electric fields. *Solid State Sci.* **2020**, *108*, 106386, https://doi.org/10.1016/j.solidstatesciences.2020.106386.
39. Toscano-Negrette, R.G.; León-González, J.C.; Vinasco, J.A.; Morales, A.L.; Koc, F.; Kavruk, A.M.; Sahin, M.; Mora-Ramos, M.E.; Sierra-Ortega, J.; Martínez-Orozco, J.C.; Restrepo, R.L.; Duque, C.A. Optical properties in a ZnS/CdS/ZnS core/shell/shell spherical quantum dot: electric and magnetic field and donor impurity effects. *Nanomaterials* **2023**, *13*, 550, https://doi.org/10.3390/nano13030550.
40. Ed-Dahmouny, A.; Zeiri, N.; Fakkahi, A.; Arraoui, R.; Jaouane, M.; Sali, A.; Es-Sbai, N.; El-Bakkari, K.; Duque, C.A. Impurity photo-ionization cross section and stark shift of ground and two low-lying excited electron-states in a core/shell ellipsoidal quantum dot. *Chem. Phys. Lett.* **2023**, *812*, 140251, https://doi.org/10.1016/j.cplett.2022.140251.
41. Shaer, A.; Hjaz, E.; Elsaid, M.K. The influence of off-centre donor impurity on the tuning of the quantum ring magnetic susceptibility. *Chem. Phys. Impact* **2023**, *6*, 100194, https://doi.org/10.1016/j.chphi.2023.100194.
42. Bala, K.J.; Peter, A.J.; Lee, C.W. Interband and intersubband optical transition energies in a $Ga_{0.7}In_{0.3}N$/*GaN* quantum dot. *Optik* **2019**, *183*, 1106-1113, https://doi.org/10.1016/j.ijleo.2019.02.074.
43. Abdi-Ben Nasrallah, S.; Bouazra, A.; Poncet, A.; Said, M. Theoretical investigation of intersubband transition energies and oscillator strength in *CdS*/SiO_2 quantum dots. *Physica E* **2010**, *43*, 146-150, https://doi.org/10.1016/j.physe.2010.06.034.
44. Safwan, S.A.; El Meshed, N. Inverse parabolic quantum dot: The transition energy under magnetic field effect. *Superlattices and Microstructures* **2016**, *96*, 282-288, https://doi.org/10.1016/j.spmi.2016.05.017.

45. Safwan, S.A.; El Meshed, N. Effect of lateral electric field on the transition energies of heavy hole state and light hole state in a semiconductor quantum dot. *J. Electronic Materials* **2019**, *48*, 6716-6723, https://doi.org/10.1007/s11664-019-07477-z.
46. Cao, S.; Tang, J.; Gao, Y.; Sun, Y.; Qiu, K.; Zhao, Y.; He, M.; Shi, J.-A.; Gu, L.; Williams, D.A.; Sheng, W.; Jin, K.; Xu, X. Longitudinal wave function control in single quantum dots with an applied magnetic field. *Scientific Reports* **2015**, *5*, 8041, https://doi.org/10.1038/srep08041.
47. Mese, A.I. The normalized transition energies between ground (*1s*) and first excited (*1p*) states in a *GaAs*/$Ga_{1-x}Al_xAs$ spherical quantum dot (SQD). *Superlattices and Microstructures* **2021**, *156*, 106932, https://doi.org/10.1016/j.spmi.2021.106932.
48. Kostic, R.; Stojanovic, D. Intersubband transitions in spherical quantum dot quantum well nanoparticle. *Optical and Quantum Electronics* **2020**, *52*, 110, https://doi.org/10.1007/s11082-020-02336-2.
49. Deyasi, A.; Bhattacharyya, S.; Das, N.R. Computation of intersubband transition energy in normal and inverted core shell quantum dots using finite difference technique. *Superlattices and Microstructures* **2013**, *60*, 414-425, https://doi.org/10.1016/j.spmi.2013.05.026.
50. Vorobiev, Yu.V.; Torchynska, T.V.; Horley, P.P. Effect of aspect ratio on energy of optical transitions in a pyramid-shaped quantum dot. *Physica E* **2013**, *51*, 42-47, https://doi.org/10.1016/j.physe.2013.02.003.
51. Deyasi, A.; Bhattacharyya, S. Interband transition energy of circular quantum dots under transverse magnetic field. *Physics Procedia* **2014**, *54*, 118-126, https://doi.org/10.1016/j.phpro.2014.10.047.
52. Jasmine, P.C.L.; Peter, A.J.; Lee, C.W. Intersubband optical transition energy in a *CdTe*/$Zn_{0.2}Cd_{0.8}Te$/*ZnTe* core/shell/shell spherical quantum dot with Smorodinsky-Winternitz confinement potential. *Chem. Phys.* **2015**, *452*, 40-45, https://doi.org/10.1016/j.chemphys.2015.02.013.
53. Çakır, B.; Atav, Ü.; Yakar, Y.; Özmen, A. Calculation of Zeeman Splitting and Zeeman transition energies of spherical quantum dot in uniform magnetic field. *Chem. Phys.* **2016**, *475*, 61-68, https://doi.org/10.1016/j.chemphys.2016.06.010.
54. Mese, A.I.; Cicek, E.; Ozkapi, S.G.; Ozkapi, B.; Erdogan, I. Calculation of intradonor normalized transition energy in spherical quantum dots made of different materials. *Physica Status Solidi B* **2023**, *260*, 2300133, https://doi.org/10.1002/pssb.202300133.
55. Xie, W. Third-order nonlinear optical susceptibility of a donor in elliptical quantum dots. *Superlattices and Microstructures* **2013**, *53*, 49-54, https://doi.org/10.1016/j.spmi.2012.09.009.
56. Xie, W. Optical anisotropy of a donor in ellipsoidal quantum dots. *Physica B* **2012**, *407*, 4588-4591, https://doi.org/10.1016/j.physb.2012.08.023.
57. Safarpour, Gh.; Izadi, M.A.; Novzari, M.; Niknam, E.; Moradi, M. Anisotropy effect on the nonlinear optical properties of a three-dimensional quantum dot confined at the center of a cylindrical nano-wire. *Physica E* **2014**, *59*, 124-132, https://doi.org/10.1016/j.physe.2014.01.007.
58. Safarpour, Gh.; Izadi, M.A.; Novzari, M.; Yazdanpanahi, S. Anisotropy effect on the linear and nonlinear optical properties of a laser dressed donor impurity in a *GaAs*/*GaAlAs* nanowire superlattice. *Superlattices and Microstructures* **2014**, *75*, 936-947, https://doi.org/10.1016/j.spmi.2014.09.018.
59. Dane, C.; Akbas, H.; Guleroglu, A.; Minez, S.; Kasapoglu, K. The hydrostatic pressure and electric field effects on the normalized binding energy of hydrogenic impurity in a *GaAs*/*AlAs* spherical quantum dot. *Physica E* **2011**, *44*, 186-189, https://doi.org/10.1016/j.physe.2011.08.012.
60. Lu, L.; Xie, W.; Shu, Z. Combined effects of hydrostatic pressure and temperature on nonlinear properties of an exciton in a spherical quantum dot under the applied electric field. *Physica B* **2011**, *406*, 3735-3740, https://doi.org/10.1016/j.physb.2011.06.081.